

Effect of dark matter on galactic black hole ringdown waveforms and shadows

Ramin G. Daghighi¹ and Gabor Kunstatter²

¹*Natural Sciences Department, Metropolitan State University, Saint Paul, Minnesota, USA 55106*

²*Physics Department, University of Winnipeg, Winnipeg, Manitoba, Canada R3B 2E9*

 (Received 9 September 2023; accepted 13 March 2024; published 4 April 2024)

We calculate the effect of dark matter on the ringdown waveform and shadow of supermassive black holes at the core of galaxies. Our main focus is on the supermassive black hole at the core of M87, which is large enough to allow for viable observational data. We compare the effects of a dark matter spike to those expected from a galactic halo of the same mass. Our calculation for the halo starts from the Hernquist density function and assumes anisotropic pressure that is zero in the radial direction. The resulting Tolman-Oppenheimer-Volkoff equations allow the corresponding metric to be obtained analytically in closed form. The geometry of the anisotropic dark matter spike is the same as that obtained in [Astrophys. J. **940**, 33 (2022)] under the assumption of isotropy. The effect of the spike is orders of magnitude more significant than the halo as long as the distribution scale of the latter is within a few orders of magnitude of the value expected from observations. Our results indicate that the impact of the spike surrounding M87* on the ringdown waveform may in principle be detectable. Finally, we point out the somewhat surprising fact that existing Event Horizon Telescope observations of black hole shadows are within an order of magnitude from being able to detect, or rule out, the presence of a spike.

DOI: [10.1103/PhysRevD.109.083004](https://doi.org/10.1103/PhysRevD.109.083004)

I. INTRODUCTION

Dark matter (DM) halos are known to surround most, if not all, supermassive black holes at the center of galaxies. It has been proposed that DM spikes exist at the core of galactic halos [1–4]. Several papers [5–12] have recently derived the effects of DM spikes on the gravitational waves emitted from black holes, but until recently the prospect of detecting these waves from supermassive black holes has been remote. This has now changed due to recent experimental developments.

The North American Nanohertz Observatory for Gravitational Waves (NANOGrav) [13], Parkes Pulsar Timing Array (PPTA) [14], and European Pulsar Timing Array (EPTA) [15] have found a common background noise at frequencies around 10^{-8} Hz. The very recent observations of Hellings–Downs correlations by the Chinese Pulsar Timing Array (CPTA) collaboration [16], EPTA collaboration [17], NANOGrav collaboration [18] and PPTA collaboration [19] strongly suggest a stochastic gravitational-wave origin of this background noise. Supermassive black hole binaries are among the main candidates to produce this background gravitational wave in the nHz range. A recent paper [20] has looked for signatures of DM spikes surrounding supermassive black holes in this data. Although these observations are still very far from being able to measure ringdown waveforms from individual supermassive black holes, it is nonetheless important to determine accurately the effect of the DM distributions on these waveforms.

Another important gravitational signature of black holes, namely the radius of the photon ring, has recently been measured for M87 using the remarkable images of the central black hole’s shadow obtained by the Event Horizon Telescope [21]. Moreover, the authors of [22] used novel statistical methods to reduce the error in this measurement to approximately 1%, leading to the possibility that measurements of the photon ring might one day yield information about the DM distribution surrounding supermassive black holes.

The shadow size of the galactic black hole Sagittarius A* (Sgr A*) in the presence of a DM spike was investigated in [23].¹ In a more recent paper [26], the present authors studied the impact of the DM spike on ringdown waveforms for the supermassive black holes Sgr A* and M87*. Using an approach similar to that of [26] in solving the Tolman-Oppenheimer-Volkoff (TOV) equations, the authors of [27] calculated the quasinormal modes (QNMs) that dominate the gravitational ringdown process of perturbed black holes surrounded by DM spikes. In these previous papers, the calculations were done in terms of the Schwarzschild time of the central black hole as measured by an observer located between the black hole event horizon and the inner radius of the spike.

¹Similar calculations for the shadow size of black holes surrounded by DM halos were done in [24,25].

In the following, we calculate the effect of DM spikes on the ringdown waveforms and shadows of the supermassive black holes at the center of the Milky Way and M87 galaxies. We emphasize the importance of expressing the results in the frame of an asymptotic stationary observer for obtaining the correct predictions.² Using the Schwarzschild time within the inner radius of the spike effectively neglects an overall redshift factor that provides the dominant contribution. Ignoring this redshift, as done in [26], underestimates considerably the size of the effect.

In addition, using the method developed in [26] combined with the redshift, we construct the spacetime for a black hole surrounded by a DM halo in order to compare its impact to the spike case. To do this, we start with the Hernquist density profile [28], which describes the distribution of DM halos in elliptical galaxies such as M87.

Two possible assumptions about the DM pressure have been used to reduce the problem of determining the spacetime geometry to that of solving the standard TOV equations. One of these (see [23,26]) is the assumption of isotropy. Isotropic pressure is however suspect in the case of noninteracting dust since near the photon sphere, where the motion is highly relativistic, nonzero radial pressure necessarily implies a flow of matter into the black hole and renders the solution nonstatic.³ The assumption of isotropy can nonetheless be viable in certain regions of the dark matter halo [29,30] and in certain scenarios such as self-interacting dark matter spikes [31]. The second, more physical, assumption is the anisotropic DM with zero radial pressure and nonzero uniform pressure tangential to spheres of constant radius. We will show in the following that the TOV equations imply the same geometry to a high degree of accuracy for both assumptions when the spike density profile is near the range previously determined by observation.

In [32], Cardoso *et al.* found an analytic solution for a Hernquist-like density profile for an anisotropic DM halo (with zero radial pressure) surrounding a black hole.⁴ In their solution, Cardoso *et al.* modify the Hernquist density function in order to impose the boundary condition $g_{tt}(r \rightarrow \infty) \rightarrow 1$, where $g_{tt}(r)$ is the metric function. While the two approaches are different, the solution of [32] turns out to be a close match to the solution we find without altering the Hernquist density function.

In the context of shadows, we confirm that the presence of a DM spike/halo increases the size of the black hole shadow [23,26]. We point out that for the spike density

estimated in [26],⁵ based on the observational data provided in [34], the increase of the shadow size due to a DM spike can be of the order of 0.1%. This calculation has taken on new significance given the recent results of [22] for M87. The increase in the shadow size is just one order of magnitude less than the proposed error bars of [22].

The paper is organized as follows. Section II reviews the general derivation of the metric for both the isotropic and anisotropic cases and describes the subtleties associated with the choice of reference frame. Section III derives the wave equation, which is covariant under the corresponding change of frame. The resulting solution for the waveform is a scalar whose shape depends on the choice of coordinates. Section IV presents a discussion of galactic black holes with DM spikes and their associated ringdown waveforms. Section V derives the metric for a dark matter halo described by the Hernquist profile. The effects of the halo on the QNM potential, due to the redshift, are then compared to those expected from a DM spike of the same mass. Section VI reviews the shadow calculations and conclusions are given in Sec. VII. The Appendix is devoted to deriving an approximate expression for the discontinuities in the QNM potential that necessarily exist at the boundaries of a DM spike. The discontinuities are proportional to the change in matter density at the boundaries and negligibly small for the proposed spike profiles.

II. DERIVING THE SPACETIME METRIC

In order to calculate ringdown waveforms that might emerge from compact objects, one first needs to determine the static background metric based on the conjectured matter content surrounding the object. We are thinking here of DM halos/spikes. This requires solving the TOV equations with appropriate boundary conditions.

One starts with the most general 4-D spherically symmetric static metric (up to coordinate transformations)

$$ds^2 = -A(r)dt^2 + B(r)^{-1}dr^2 + r^2d\Omega^2 \\ = -e^{\mu(r)}dt^2 + \left(1 - \frac{2M(r)}{r}\right)^{-1}dr^2 + r^2d\Omega^2, \quad (1)$$

where we use geometric units with $c = G = 1$. For asymptotically flat metrics, $e^{\mu(r)} \rightarrow \text{constant}$ at spatial infinity. This constant is normally chosen to be unity, thereby fixing the time coordinate to be the proper time of a stationary asymptotic observer. This is the correct choice when comparing waves emitted by distant compact objects, despite the fact that it has not always been used in recent discussions of ringdown waveforms.

²The authors are grateful to Andrei Frolov for illuminating discussions in this regard.

³We are grateful to Don Page for bringing this argument to our attention.

⁴For spacetime solutions for other DM halo density profiles, see [33].

⁵We note a typo in Eqs. (30) and (31) of [26], where the authors estimate the DM spike density based on observational data. More specifically, the term $(1 + r_0/r)$ should be $(1 + r/r_0)$. The numerical results, however, are correct.

We now outline the derivation of the metric in the spacetime containing a general anisotropic, extended but finite, spherical shell of matter surrounding a black hole. See [26] for more details on the derivation. We denote the inner radius of the shell by r_{in} and the outer radius by r_{out} . Assume a spherically symmetric anisotropic perfect fluid stress tensor for the shell of matter

$$T_{\nu}^{\mu} = \text{diag}(\rho(r), p_r(r), p_t(r), p_t(r)), \quad (2)$$

where p_r is the pressure in the radial direction and p_t denotes the pressure tangential to a symmetric two sphere at fixed radius, r . The resulting equations in the shell region are

$$G_{tt} = 0 \Rightarrow \frac{dM(r)}{dr} = 4\pi r^2 \rho(r) \quad (3)$$

$$G_{rr} = 0 \Rightarrow \frac{d\mu(r)}{dr} = 2 \frac{M(r) + 4\pi r^3 p_r(r)}{r[r - 2M(r)]} \quad (4)$$

$$\begin{aligned} \nabla_{\nu} T^{r\nu} = 0 &\Rightarrow \frac{dp_r(r)}{dr} \\ &= -[\rho(r) + p_r(r)] \frac{M(r) + 4\pi r^3 p_r(r)}{r[r - 2M(r)]} + \frac{2}{r}(p_t - p_r). \end{aligned} \quad (5)$$

Two different cases have been considered in the recent literature.

The first case is the isotropic case, where $p_t(r) = p_r(r) = p(r)$. Equations (3) and (4) remain unchanged, except that p_r is replaced by $p(r)$ in the latter. The momentum conservation equation becomes

$$\nabla_{\nu} T^{r\nu} = 0 \Rightarrow \frac{dp(r)}{dr} = -[\rho(r) + p(r)] \frac{M(r) + 4\pi r^3 p(r)}{r[r - 2M(r)]}. \quad (6)$$

Equations (3), (4), and (6) are the standard spherical TOV equations found in textbooks (see [35] for example). They are rather difficult to solve in general because of the presence of $p(r)$ in both (4) and (6).

The second case is the anisotropic case considered in [32,33] with zero radial pressure ($p_r = 0$). Equation (3) again remains unchanged, while the remaining equations simplify to

$$G_{rr} = 0 \Rightarrow \frac{d\mu(r)}{dr} = 2 \frac{M(r)}{r[r - 2M(r)]} \quad (7)$$

$$\nabla_{\nu} T^{r\nu} = 0 \Rightarrow 0 = -\rho(r) \frac{M(r)}{r[r - 2M(r)]} + \frac{2}{r} p_t. \quad (8)$$

In this case, Eq. (7) can be integrated directly while Eq. (8) can be solved algebraically once $M(r)$ is determined

from (3). Note that one does not need to know the transverse pressure to determine the metric.

In both cases there are three equations in four unknowns, either $[\mu(r), M(r), \rho(r), p(r)]$ or $[\mu(r), M(r), \rho(r), p_t(r)]$, which means they need to be supplemented by a fourth equation. Normally this is taken to be the equation of state relating the density to the pressure. In the cases we are interested in, such as DM halos/spikes, theoretical calculations [2] predict a particular density profile for the shell. This provides the extra equation. Therefore, there is no freedom left to specify the equation of state.

To solve the isotropic case, we will assume for the simplicity that the pressure term is negligible when solving for $\mu(r)$ in Eq. (4). The validity of this assumption, in the case of DM spikes, was proven in [26] and is confirmed again here. As long as the pressure term is negligible in Eq. (4), it should be clear that, for a given density function, there is no difference in geometry for the isotropic case and the anisotropic case. This is a direct consequence of the fact that in both cases the pressure is irrelevant to the determination of the geometry, albeit for very different physical reasons.

Thus, in both cases, given the density profile, one can obtain the mass function by integrating Eq. (3) from r_{BH} to spatial infinity with the boundary condition that $M(r < r_{\text{in}}) = M_{\text{BH}}$, where we use r_{BH} and M_{BH} to indicate the horizon radius and mass of the central black hole respectively. Given the mass function obtained above, one integrates Eq. (4) to get the second metric function $\mu(r)$. Since the TOV equations are first order, each requires the specification of a single boundary condition in order to provide a unique solution. For Eq. (3), the correct boundary condition is that $M(r < r_{\text{in}}) = M_{\text{BH}}$. Equivalently, one can choose $M(r \geq r_{\text{out}}) = M_{\text{total}} = M_{\text{BH}} + M_{\text{shell}}$, where M_{shell} is the total mass of the shell. Since the tangential metric must be continuous at the boundaries for the surface geometry on the boundary to be uniquely defined, there is no freedom in the choice of boundary conditions. A potential subtlety does arise in the choice of boundary condition for $g_{tt}(r)$ [and consequently for $\mu(r)$] in Eq. (4), which in turn determines the time coordinate. The obvious choice is that $g_{tt}(r) \rightarrow 1$ ($\mu(r) \rightarrow 0$) far from the black hole so that t is the proper time of an asymptotic observer at rest relative to the black hole. This is presumably the frame in which the measurements of the ringdown waveform and shadow are made. On the other hand, it is useful to consider the ringdown waveforms caused by outgoing waves that originate in the vacuum region $r < r_{\text{in}}$, where the initial data are specified. Such outgoing boundary conditions are preferred for two reasons: first, they are in some sense more physical since the ringdown waveforms from the merger of binary black holes do originate from near the horizon. Secondly, numerical integrations of the wave equation yield better results (i.e., a larger number of reliable oscillations before errors set in) than simulations that start from ingoing

waves. When starting with outgoing initial data, as done in [26], it seems natural to impose the boundary condition on the metric in the shell's interior, namely

$$g_{tt}(r < r_{\text{in}}) = 1 - \frac{2M_{\text{BH}}}{r}, \quad (9)$$

which is the Schwarzschild metric of the central black hole.

Following [26] we integrate outward starting at r_{in} with the boundary condition (9), which fixes the time coordinate t to be the Schwarzschild time of the vacuum metric associated with the central black hole. In this case, t is what would be the proper time of a stationary observer at infinity had the DM spike not been present. This is not the same as the actual proper time of an asymptotic observer when the spike is present. It is the latter proper time with respect to which measurements will be taken. We can rewrite Eq. (9) in terms of $\mu(r)$ as

$$\mu(r < r_{\text{in}}) = \ln \left(1 - \frac{2M_{\text{BH}}}{r} \right), \quad (10)$$

where clearly $\mu(r) \rightarrow 0$ as $r \rightarrow \infty$.

The integration of Eq. (4) proceeds to larger radii with the assumption that the metric function be continuous at both shell boundaries. This is required to ensure that the shell boundary has a well-defined geometry.⁶ In the shell region $r_{\text{in}} \leq r < r_{\text{out}}$, we find the metric function to be

$$\mu(r) = \ln \left(1 - \frac{2M_{\text{BH}}}{r_{\text{in}}} \right) + \int_{r_{\text{in}}}^r dr \frac{2M(r)}{r(r - 2M(r))}. \quad (11)$$

To obtain a solution that is continuous at the outer radius of the shell, we extend the integral in Eq. (11) past r_{out} as follows:

$$\begin{aligned} \mu(r \geq r_{\text{out}}) &= \ln \left(1 - \frac{2M_{\text{BH}}}{r_{\text{in}}} \right) + \int_{r_{\text{in}}}^{r_{\text{out}}} dr \frac{2M(r)}{r(r - 2M(r))} \\ &+ \int_{r_{\text{out}}}^r dr \frac{2M_{\text{total}}}{r(r - 2M_{\text{total}})}. \end{aligned} \quad (12)$$

Note that the last integral above gives

$$\int_{r_{\text{out}}}^r dr \frac{2M_{\text{total}}}{r(r - 2M_{\text{total}})} = \ln \left(1 - \frac{2M_{\text{total}}}{r} \right) - \ln \left(1 - \frac{2M_{\text{total}}}{r_{\text{out}}} \right). \quad (13)$$

After combining Eqs. (12) and (13), we arrive at

⁶Note that $\mu(r)$ is not necessarily smooth at the boundaries. This introduces discontinuities in the QNM potential, which can be shown to be small in the present context. For details, see the Appendix.

$$\mu(r \geq r_{\text{out}}) = \ln \left(1 - \frac{2M_{\text{total}}}{r} \right) + \ln(C), \quad (14)$$

where

$$C = \frac{\left(1 - \frac{2M_{\text{BH}}}{r_{\text{in}}} \right)}{\left(1 - \frac{2M_{\text{total}}}{r_{\text{out}}} \right)} \exp \int_{r_{\text{in}}}^{r_{\text{out}}} dr \frac{M(r)}{r(r - 2M(r))}. \quad (15)$$

One thereby obtains a metric on the exterior that is asymptotically flat but for which $\mu(r)$ does not go to zero (i.e. $g_{tt}(r) \rightarrow 1$) at infinity:

$$ds^2 = -C \left(1 - \frac{2M_{\text{total}}}{r} \right) dt^2 + \left(1 - \frac{2M_{\text{total}}}{r} \right)^{-1} dr^2 + r^2 d\Omega^2. \quad (16)$$

The constant $C \neq 1$ arises due to the presence of the matter shell so that t is not the proper time of an asymptotic observer. It turns out that the constant C provides the dominant contribution to the modification of the ringdown waveform caused by the presence of the shell. The relationship between the time t in (16) and the proper time \tilde{t} of an asymptotic observer is

$$\tilde{t} = \sqrt{C}t. \quad (17)$$

This is simply a redshift factor that is a consequence of the extra mass in the system provided by the shell. For positive definite shell densities C is greater than one, so that in terms of the rescaled time \tilde{t} , the waveform appears stretched.

III. WAVE EQUATION

In terms of the Schwarzschild time t of the vacuum metric of the central black hole, the QNM wave equation has the general form

$$\left(\frac{\partial^2}{\partial t^2} - \frac{\partial^2}{\partial r_*^2} + V(r(r_*)) \right) \Psi(t, r_*) = 0, \quad (18)$$

where r_* is the tortoise coordinate defined as

$$dr_* = \frac{dr}{\sqrt{A(r)B(r)}}. \quad (19)$$

For the particular case of massless scalar perturbations, the QNM potential is

$$V(r) = A(r) \frac{l(l+1)}{r^2} + \frac{1}{2r} \frac{d}{dr} [A(r)B(r)]. \quad (20)$$

With the given potential, one then solves (18) for the wave $\Psi(t, r_*)$ with the initial condition of an outgoing wave

$$\begin{aligned}\Psi(0, r_*) &= f(r_*) \\ \partial_t \Psi(t, r_*)|_{t=0} &= -\partial_{r_*} \Psi(0, r_*),\end{aligned}\quad (21)$$

where $f(r_*)$ is usually taken to be a Gaussian function.

As explained earlier, in order to find the waveform measured by an asymptotic observer, one can first determine the waveform in terms of the Schwarzschild time t of the interior geometry ($r < r_{\text{in}}$) by solving Eq. (18) with initial conditions (21) and then rescale the time coordinate to the proper time of an asymptotic observer, $\tilde{t} = \sqrt{C}t$. Alternatively, one can do the entire calculation in terms of \tilde{t} . In the latter case, one calculates $\tilde{\mu}(r)$ by integrating inward from r_{out} with the boundary condition

$$\tilde{\mu}(r \geq r_{\text{out}}) = \ln \left(1 - \frac{2M_{\text{total}}}{r} \right). \quad (22)$$

The integration of Eq. (4) then proceeds to the shell region of $r_{\text{in}} \leq r < r_{\text{out}}$, where

$$\tilde{\mu}(r) = \ln \left(1 - \frac{2M_{\text{total}}}{r_{\text{out}}} \right) + \int_{r_{\text{out}}}^r dr \frac{2M(r)}{r(r - 2M(r))}. \quad (23)$$

Combining Eqs. (11), (15), and (23), one finds that $\tilde{\mu}(r) = \mu(r) - \ln(C)$, which means

$$\tilde{A}(r) = A(r)/C. \quad (24)$$

Therefore, the conversion of the outward integration to an inward integration suitable for an asymptotic observer can be reduced to a simple rescaling. The tortoise coordinate for the asymptotic observer is

$$d\tilde{r}_* = \frac{dr}{\sqrt{\tilde{A}(r)B(r)}} = \sqrt{C}dr_*. \quad (25)$$

In order to verify the covariance of the wave equation under time rescales, we note that

$$\tilde{V}(r) = \tilde{A}(r) \frac{l(l+1)}{r^2} + \frac{1}{2r} \frac{d}{dr} [\tilde{A}(r)B(r)] = \frac{V(r)}{C}. \quad (26)$$

Putting these transformations together we find, as expected, that

$$C \left(\frac{\partial^2}{\partial \tilde{t}^2} - \frac{\partial^2}{\partial \tilde{r}_*^2} + \tilde{V}(\tilde{r}_*) \right) \tilde{\Psi}(\tilde{t}, \tilde{r}_*) = 0, \quad (27)$$

where

$$\tilde{V}(\tilde{r}_*) = \frac{V(r(\tilde{r}_*))}{C}. \quad (28)$$

Equation (27) is of the same form as the wave equation (18). This is all simply a manifestation of the fact that the field is

a scalar, so that the wave equation is covariant and the solutions are related by

$$\tilde{\Psi}(\tilde{t}, \tilde{r}_*) = \Psi(t, r_*) = \Psi \left(\frac{1}{\sqrt{C}} \tilde{t}, \frac{1}{\sqrt{C}} \tilde{r}_* \right). \quad (29)$$

In the frame of the asymptotic observer, the same initial conditions as in Eq. (21) above take the form

$$\begin{aligned}\tilde{\Psi}(0, \tilde{r}_*) &= \tilde{f}(\tilde{r}_*) = f(r_*(\tilde{r}_*)) = f \left(\frac{1}{\sqrt{C}} \tilde{r}_* \right) \\ \sqrt{C} \partial_{\tilde{t}} \tilde{\Psi}(\tilde{t}, \tilde{r}_*)|_{\tilde{t}=0} &= -\sqrt{C} \partial_{\tilde{r}_*} \tilde{\Psi}(0, \tilde{r}_*) = \sqrt{C} \partial_{r_*} f \left(\frac{1}{\sqrt{C}} \tilde{r}_* \right).\end{aligned}\quad (30)$$

Thus Gaussian initial data specified in terms of r_* change the width by a factor of \sqrt{C} under the frame transformation. Of course, both forms correspond to the same initial data in terms of the areal radius. Although it is important to compare apples to apples with respect to initial data, numerical calculations are not sensitive to small changes to the initial wave due to the fact that black holes oscillate with natural vibrational modes (QNMs) that have unique frequencies and damping rates.

IV. GALACTIC BLACK HOLES WITH DARK MATTER SPIKES

As we mentioned earlier, the results in [26] are obtained in the Schwarzschild coordinates in the region $r < r_{\text{in}}$. In this section, we examine the same waveforms as seen by an asymptotic stationary observer.

The adiabatically formed DM spike, studied in [26], has a density profile [2]

$$\rho_{\text{DM}}^{\text{sp}}(r) \simeq \rho_{\text{sp}} \left(\frac{R_{\text{sp}}}{r} \right)^{\gamma_{\text{sp}}}, \quad (31)$$

were ρ_{sp} and R_{sp} are the density and radius, respectively, at the outer edge of the spike. The expected value for ρ_{sp} , when $\gamma_{\text{sp}} = 7/3$, is taken to be $8.00 \times 10^{-23} \text{ g cm}^{-3}$ for Sgr A (see Table 1 of [26]) and $2.12 \times 10^{-23} \text{ g cm}^{-3}$ for M87 (see Table 2 of [26]). In this section, we present the results for these cases.

To see how the DM spike influences the shape of the QNM potential given in Eq. (20), in Figs. 1, 3, and 5 we plot the Schwarzschild potential together with the potentials corresponding to the time coordinates t and \tilde{t} , respectively. Figure 1 shows the potential for Sgr A* with a DM density at the outer edge of the spike, ρ_{sp} , approximately 840 times the expected value given in Table 1 of [26] for the case of $\gamma_{\text{sp}} = 7/3$. Note that while the potential for the coordinate t closely follows the Schwarzschild case, the potential for the asymptotic observer is very different.

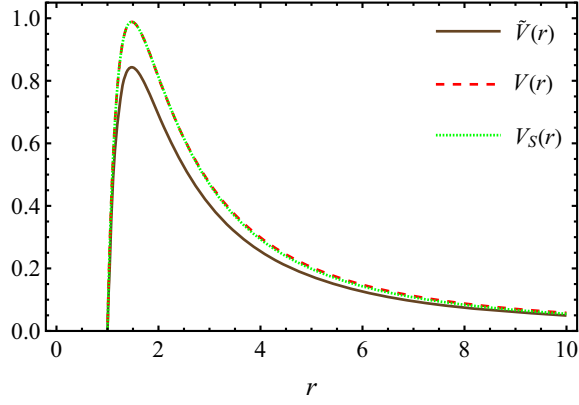


FIG. 1. Scalar QNM potential as a function of radial coordinate for $l = 2$ and $\gamma_{\text{sp}} = 7/3$ for Sgr A* with the mass of $M_{\text{BH}} = 4.1 \times 10^6 M_{\odot}$ surrounded by a DM spike. $V(r)$, in dashed red, is the potential corresponding to t and $\tilde{V}(r)$, in solid brown, is the potential viewed by an asymptotic observer. We choose $\rho_{\text{sp}} = 6.7 \times 10^{-20} \text{ g cm}^{-3}$ (≈ 840 times the expected value), $r_{\text{b}} = 2r_{\text{BH}}$ and $R_{\text{sp}} = 0.235 \text{ kpc}$. With these values, $\mathcal{C} = 1.172$. For comparison, we include the Schwarzschild potential, $V_{\text{S}}(r)$, in dotted green for $M_{\text{BH}} = 4.1 \times 10^6 M_{\odot}$. All our variables are expressed in terms of black hole parameters.

Figures 3 and 5 show the potential for M87* with $\rho_{\text{sp}} \approx 8.4$ and $\rho_{\text{sp}} \approx 84$ times the expected value, provided in Table 2 of [26] for the case of $\alpha_{\gamma} = 1.94$, respectively.

The ringdown waveforms for the potentials in Figs. 1, 3, and 5 are shown in Figs. 2, 4, and 6 respectively. These waveforms are caused by the outgoing Gaussian pulse used in [26] that initiates near the event horizon (inside the photon sphere) and gets detected after being transmitted through the QNM potential. In these figures, we also provide the ringdown waveform for the Schwarzschild case for comparison. Note that for the more massive black hole M87*, less density at the outer edge of the spike is required to achieve an observable signal. In Figs. 3 and 4,

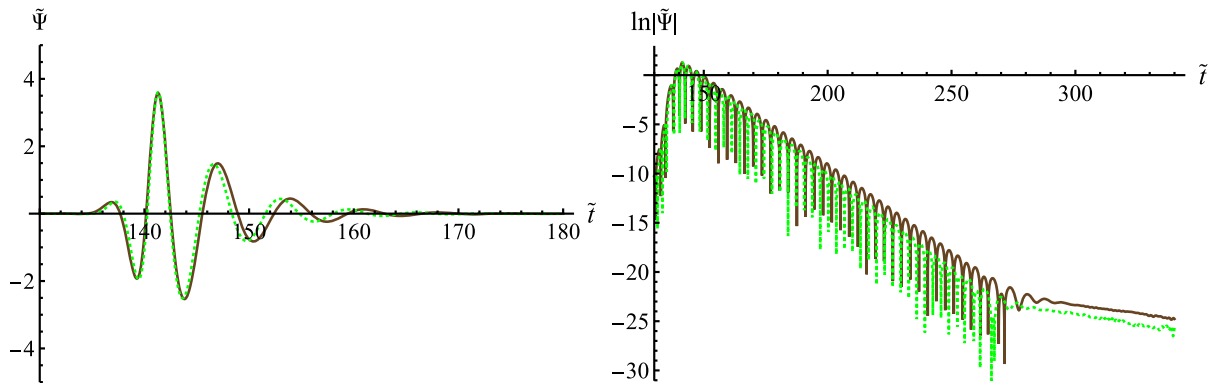


FIG. 2. In solid brown, ringdown waveform $\tilde{\Psi}$ (left) and $\ln|\tilde{\Psi}|$ (right) as a function of time \tilde{t} for the potential, $\tilde{V}(r)$, shown in solid brown in Fig. 1. For numerical purposes, we detect the waveform at $r = 80r_{\text{BH}}$. For comparison, we include the Schwarzschild ringdown waveform in dotted green. All our variables are expressed in terms of black hole parameters.

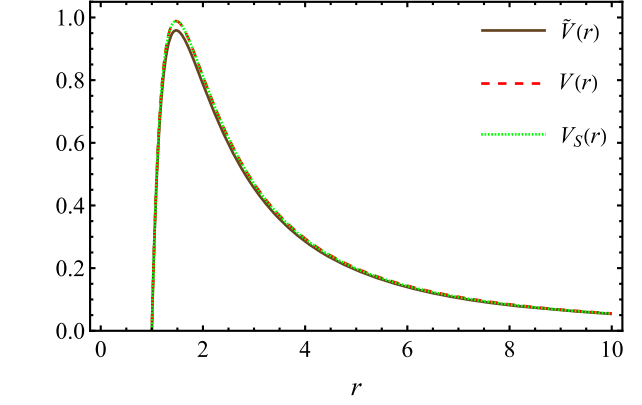


FIG. 3. Scalar QNM potential as a function of radial coordinate for $l = 2$ and $\gamma_{\text{sp}} = 7/3$ for M87* with the mass of $M_{\text{BH}} = 6.4 \times 10^9 M_{\odot}$ surrounded by a DM spike. $V(r)$, in dashed red, is the potential corresponding to t and $\tilde{V}(r)$, in solid brown, is the potential viewed by an asymptotic observer. We choose $\rho_{\text{sp}} = 1.8 \times 10^{-22} \text{ g cm}^{-3}$ (8.4 times the expected value), $r_{\text{b}} = 2r_{\text{BH}}$ and $R_{\text{sp}} = 4.26 \text{ kpc}$. With these values, $\mathcal{C} = 1.031$. For comparison, we include the Schwarzschild potential, $V_{\text{S}}(r)$, in dotted green for $M_{\text{BH}} = 6.4 \times 10^9 M_{\odot}$. All our variables are expressed in terms of black hole parameters.

the change in the potential and ringdown waveform due to the presence of DM spike is visible in the asymptotic frame even for a density as low as ≈ 8.4 times the expected ρ_{sp} . This is not the case for an observer who uses the time coordinate t .

Finally, in Fig. 7, we generate the ringdown waveform produced by the same Gaussian pulse that moves inward from a far distance outside the potential $\tilde{V}(r)$ shown in Fig. 5 and reflects back to generate the ringdown waveform. The reflected wave produces considerably fewer oscillations than the transmitted wave shown in Fig. 6. However, the transmitted and reflected waves are consistent in terms of the observed impact of the DM spike. In both cases, the main contribution to the waveform

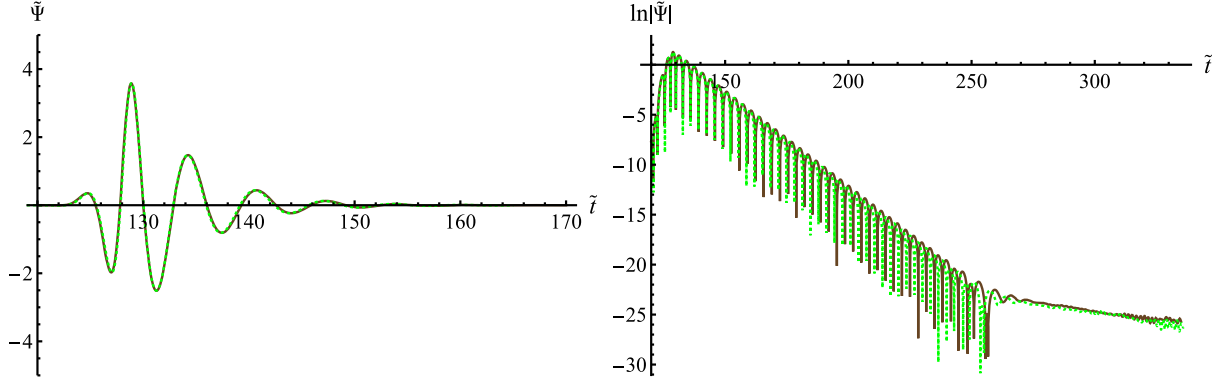


FIG. 4. In solid brown, ringdown waveform $\tilde{\Psi}$ (left) and $\ln|\tilde{\Psi}|$ (right) as a function of time \tilde{t} for the potential, $\tilde{V}(r)$, shown in solid brown in Fig. 3. For numerical purposes, we detect the waveform at $r = 80r_{\text{BH}}$. For comparison, we include the Schwarzschild ringdown waveform in dotted green. All our variables are expressed in terms of black hole parameters.

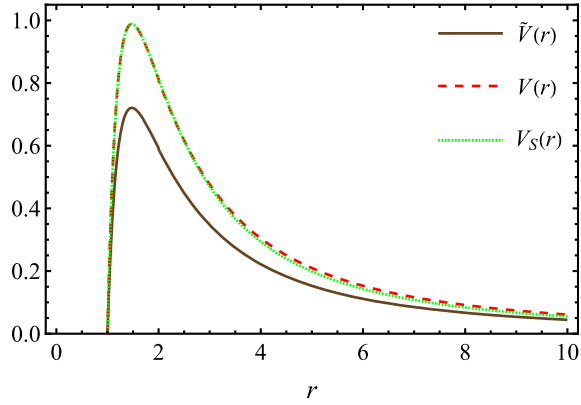


FIG. 5. Scalar QNM potential as a function of radial coordinate for $l = 2$ and $\gamma_{\text{sp}} = 7/3$ for M87* with the mass of $M_{\text{BH}} = 6.4 \times 10^9 M_{\odot}$ surrounded by a DM spike. $V(r)$, in dashed red, is the potential corresponding to t , and $\tilde{V}(r)$, in solid brown, is the potential viewed by an asymptotic observer. We choose $\rho_{\text{sp}} = 1.8 \times 10^{-21} \text{ g cm}^{-3}$ (84 times the expected value), $r_{\text{b}} = 2r_{\text{BH}}$ and $R_{\text{sp}} = 4.26 \text{ kpc}$. With these values, $\mathcal{C} = 1.371$. For comparison, we include the Schwarzschild potential, $V_S(r)$, in dotted green for $M_{\text{BH}} = 6.4 \times 10^9 M_{\odot}$. All our variables are expressed in terms of black hole parameters.

modification comes from the redshift caused by the extra mass in the system.

Note that it is not possible numerically to generate these ringdown waveforms for an observer at a region outside the spike, since R_{sp} is of the order of at least 10^7 times the black hole radius. However, the potential drops very quickly with distance. For example, at $r = 50r_{\text{BH}}$ the potential is three orders of magnitude smaller than its value at the peak. This allows us to generate the ringdown waveform for an observer located at a radius close to the black hole (roughly around $80r_{\text{BH}}$). Since the potential is already relatively small at this radius, we do not expect any significant modification in the waveform as it travels all the way to the region outside the spike.

It is evident from the results in this section that the impact of the DM spike on the ringdown waveform is more pronounced in the frame of an asymptotic observer, compared to the results presented in [26]. More specifically, to generate roughly the same modification in the ringdown waveform, we need an order of magnitude less DM density in terms of the proper time \tilde{t} of an asymptotic observer compared to an observer who uses t . We can, therefore, conclude that if a significant gravitational wave detection associated with perturbations of a black hole with a mass comparable to M87* occurs, it might provide the means to detect the presence of a DM spike or at least put a model dependent bound on its parameters. More massive galactic black holes could likely yield even clearer signals, as argued in [26].

V. GALACTIC BLACK HOLES WITH DARK MATTER HALOS

In this section, we investigate a black hole surrounded by a DM halo in order to compare our results with the spike case. Since the observational signal is more significant for larger black holes, we focus on M87*. The density function of the DM halo in an elliptical galaxy, such as M87, is well-described by the Hernquist profile that has the form [28]

$$\rho(r) = \frac{M_{\text{halo}} a_0}{2\pi r (r + a_0)^3}, \quad (32)$$

where M_{halo} is the total mass of the halo and a_0 is the scale radius. The scale radius of a halo is typically of the order $a_0 \approx 10^4 M_{\text{halo}}$ [36]. After integrating the TOV equation (3) with the above density profile, we obtain

$$M(r) = M_{\text{total}} - M_{\text{halo}} a_0 \frac{2r + a_0}{(r + a_0)^2}, \quad (33)$$

where we choose the constant of integration to be $M_{\text{total}} = M_{\text{BH}} + M_{\text{halo}}$.

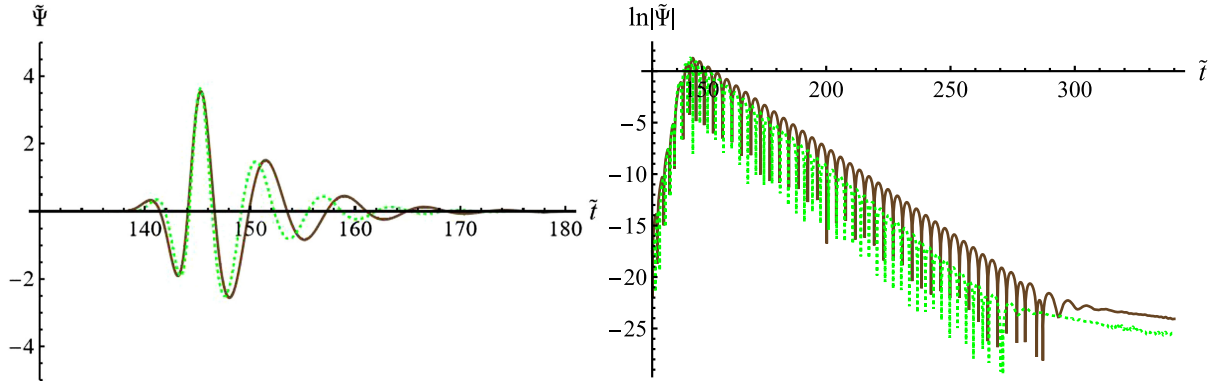


FIG. 6. In solid brown, ringdown waveform $\tilde{\Psi}$ (left) and $\ln|\tilde{\Psi}|$ (right) as a function of time \tilde{t} for the potential, $\tilde{V}(r)$, shown in solid brown in Fig. 5. For numerical purposes, we detect the waveform at $r = 70r_{\text{BH}}$. For comparison, we include the Schwarzschild ringdown waveform in dotted green. All our variables are expressed in terms of black hole parameters.

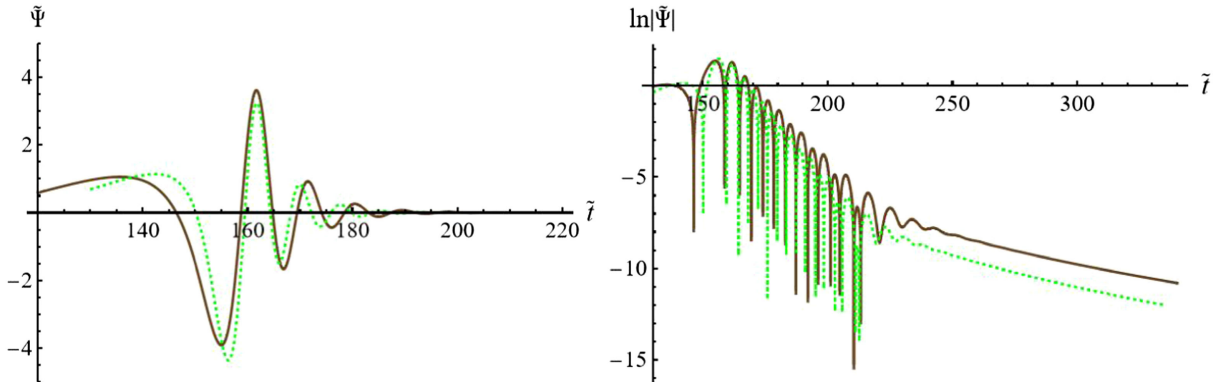


FIG. 7. In solid brown, ringdown waveform $\tilde{\Psi}$ (left) and $\ln|\tilde{\Psi}|$ (right) as a function of time \tilde{t} for the potential, $\tilde{V}(r)$, shown in solid brown in Fig. 5. Unlike all the other figures, the ringdown is produced by an ingoing pulse starting at $r \approx 41r_{\text{BH}}$. For numerical purposes, we detect the waveform at $r = 70r_{\text{BH}}$. For comparison, we include the Schwarzschild ringdown waveform in dotted green. All our variables are expressed in terms of black hole parameters.

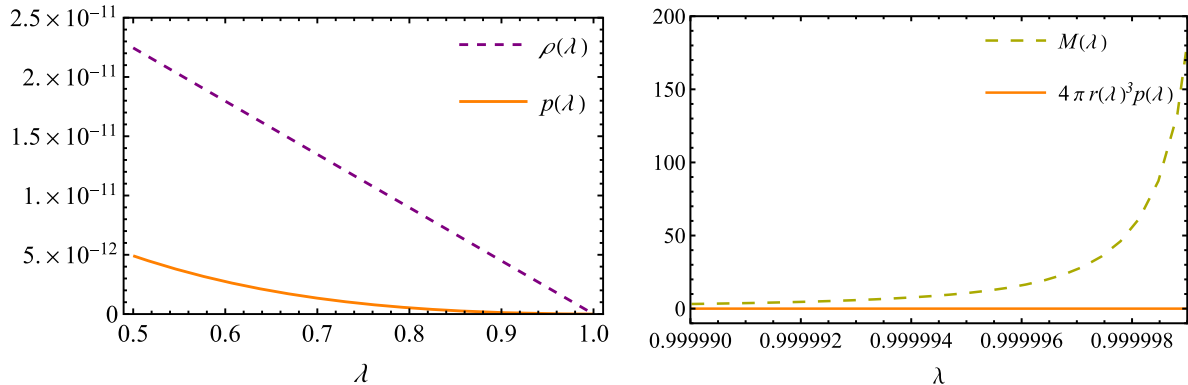


FIG. 8. On the left, the DM halo pressure p as a function of $\lambda = 1 - 2M_{\text{BH}}/r$ is plotted in solid orange for $a_0 = 1000M_{\text{halo}}$, where $M_{\text{halo}} = 4.54 \times 10^{13}M_{\odot}$. The pressure is obtained numerically using Eq. (6). For comparison, we include the DM halo density $\rho(\lambda)$ in dashed purple. On the right, for the same parameters, we plot the term $4\pi r(\lambda)^3 p(\lambda)$ and $M(\lambda)$ to show that the pressure term stays negligible while $M(\lambda)$ increases from M_{BH} to M_{total} as λ approaches 1 ($r \rightarrow \infty$). All our variables are expressed in terms of black hole parameters.

In the anisotropic case with negligible radial pressure, p_r , one can proceed to Eq. (34) below. In the isotropic case, which is physically less relevant, we need to solve Eq. (6) for $p(r)$. This is not possible analytically, but we have solved it numerically using the built-in *Mathematica* commands for solving differential equations. It turns out that the pressure term, $4\pi r^3 p(r)$, can be neglected compared to $M(r)$ in the TOV equations. We show the numerical results in Fig. 8 for the case where $a_0 = 1000M_{\text{halo}}$. To better manage the numerical calculations, we solve Eq. (5) in the coordinate $\lambda = 1 - 2M_{\text{BH}}/r$, which maps the interval $r_{\text{BH}} \leq r < \infty$ to $0 \leq \lambda < 1$. While

pressure and density are comparable in magnitude, it is clear from Fig. 8 that $4\pi r^3 p(r) \ll M(r)$. More specifically, the term $4\pi r^3 p(r)$ stays close to zero while $M(r)$ increases from M_{BH} to M_{total} at large distances from the black hole.

In the absence of pressure, anisotropic and isotropic cases become the same. This is because for both cases the TOV equation (4) reduces to Eq. (7). Combining Eqs. (7) and (33) gives

$$\frac{d\mu(r)}{dr} = -\frac{1}{r} + \frac{1}{r - 2[M_{\text{total}} - M_{\text{halo}}a_0 \frac{2r+a_0}{(r+a_0)^2}]}. \quad (34)$$

We integrate Eq. (34) to get

$$\begin{aligned} \mu(r) &= -\int \frac{dr}{r} + \int \frac{y^2 dy}{y^3 - (2M_{\text{total}} + a_0)y^2 + 4M_{\text{halo}}a_0y - 2M_{\text{halo}}a_0^2} + C \\ &= -\int \frac{dr}{r} + \frac{y_0^2}{y_1y_2 + y_0(y_0 - y_1 - y_2)} \int \frac{dy}{y - y_0} \\ &\quad + \frac{1}{y_1y_2 + y_0(y_0 - y_1 - y_2)} \int \frac{(y_0y_1y_2 - y_0y_1y - y_0y_2y + y_1y_2y)dy}{y^2 - (y_1 + y_2)y + y_1y_2} + C, \end{aligned} \quad (35)$$

where we have used the change of variable $y = r + a_0$. Here, y_0 is the real root of the equation $y^3 - (2M_{\text{total}} + a_0)y^2 + 4M_{\text{halo}}a_0y - 2M_{\text{halo}}a_0^2$ and y_1 and y_2 are the two complex conjugate roots. After integration, the final result for the metric function, $A(r) = e^{\mu(r)}$, is

$$\begin{aligned} A(r) &= \left(1 - \frac{2M_{\text{BH}}}{r_{\text{in}}}\right) \frac{r_{\text{in}}}{r} \left(\frac{r + a_0 - y_0}{r_{\text{in}} + a_0 - y_0}\right)^{\frac{y_0^2}{y_1y_2 + y_0(y_0 - y_1 - y_2)}} \left(\frac{(r + a_0)^2 - (y_1 + y_2)(r + a_0) + y_1y_2}{(r_{\text{in}} + a_0)^2 - (y_1 + y_2)(r_{\text{in}} + a_0) + y_1y_2}\right)^{\frac{[y_1y_2 - y_0(y_1 + y_2)]}{2[y_1y_2 + y_0(y_0 - y_1 - y_2)]}} \\ &\quad \times e^{\frac{2y_0y_1y_2 - y_0(y_1 + y_2)^2 + y_1y_2(y_1 + y_2)}{4y_1y_2 - (y_1 + y_2)^2} \left(\arctan \frac{2(r+a_0) - y_1 - y_2}{\sqrt{4y_1y_2 - (y_1 + y_2)^2}} - \arctan \frac{2(r_{\text{in}}+a_0) - y_1 - y_2}{\sqrt{4y_1y_2 - (y_1 + y_2)^2}}\right)}. \end{aligned} \quad (36)$$

We have chosen the constant of integration, C , so that $A(r_{\text{in}}) = 1 - 2M_{\text{BH}}/r_{\text{in}}$.

Using Eqs. (15), (33), and (36) we can obtain the scalar QNM potential (26) for the DM halo. We show the scalar QNM potential, $\tilde{V}_{\text{halo}}(r)$, for different values of a_0 in Fig. 9. The QNM potential of the halo is only comparable to the spike of the same mass for $a_0 = 10M_{\text{halo}}$. In this case, approximately 99% of the halo mass is contained in the spike region of $r_{\text{in}} \leq r < r_{\text{out}}$. For larger values of a_0 , the mass of the halo spreads out further from the black hole and the QNM potential becomes almost indistinguishable from the Schwarzschild case (black hole with no DM) for $a_0 > 100M_{\text{halo}}$. In other words, the impact of the redshift on the QNM potential is negligible for a halo as long as its distribution scale is within a few orders of magnitude of the value expected from observations. This indicates the

observational signal does depend on how DM is distributed around a black hole.

In [32], Cardoso *et al.* have also found an analytic solution for a Hernquist-like density profile for an anisotropic DM halo, with negligible p_r , surrounding a black hole. In their solution, Cardoso *et al.* modify the Hernquist density function in order to impose the boundary condition $g_{tt}(r \rightarrow \infty) \rightarrow 1$. The solution of [32] turns out to be a close match to the solution we find here, where we do not alter the Hernquist density function. In Fig. 10, we show the difference between the scalar QNM potential obtained using our metric functions (33) and (36) and the potential found using the metric functions provided in [32]. The difference between the two solutions is less than 0.1%.

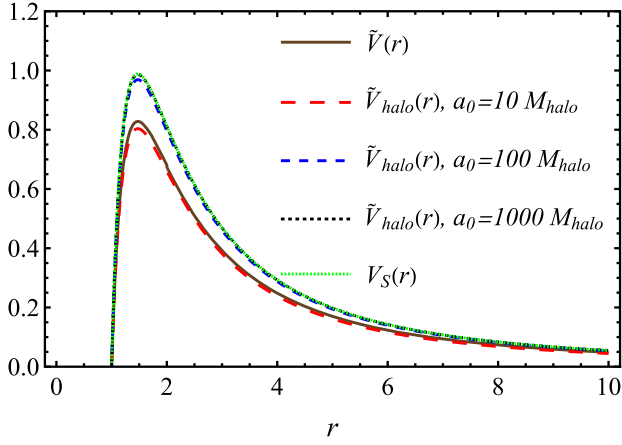


FIG. 9. Scalar QNM potential as a function of radial coordinate for $l = 2$ for M87* with the mass of $M_{\text{BH}} = 6.4 \times 10^9 M_{\odot}$ surrounded by a DM halo with the mass of $M_{\text{halo}} = 4.54 \times 10^{13} M_{\odot}$. The halo extends from $r_{\text{in}} = 2r_{\text{BH}}$ to infinity. $\tilde{V}_{\text{halo}}(r)$ is plotted for $a_0 = 10M_{\text{halo}}$, $a_0 = 100M_{\text{halo}}$, and $a_0 = 1000M_{\text{halo}}$ in dashed red, dashed blue, and dashed black respectively. For comparison, we also plot $\tilde{V}(r)$ in solid brown for a DM spike with the same mass, which extends between $r_{\text{in}} = 2r_{\text{BH}}$ and $r_{\text{out}} = 4.26$ kpc. We choose the same r_{out} for the DM halo to calculate the redshift factor. This assumes the observer is located at $r = r_{\text{out}}$. Choosing $r_{\text{out}} \sim \infty$ changes the results by only 0.1%. In addition, we include the Schwarzschild potential, $V_S(r)$, in dotted green for $M_{\text{BH}} = 6.4 \times 10^9 M_{\odot}$. All our variables are expressed in terms of black hole parameters.

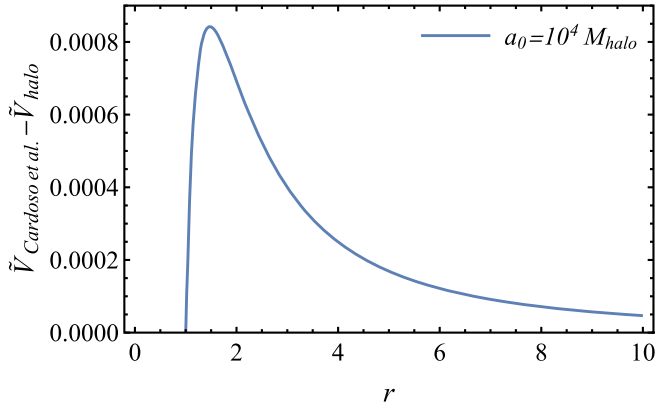


FIG. 10. The difference between the scalar QNM potential for $l = 2$ obtained using the metric functions derived in this paper and the DM halo model suggested by Cardoso *et al.* [32] is shown for $M_{\text{BH}} = 6.4 \times 10^9 M_{\odot}$ and $M_{\text{halo}} = 4.54 \times 10^{13} M_{\odot}$.

VI. SHADOW RADIUS

We summarize the shadow calculations as follows.⁷ Consider the action for particle geodesics

$$S = \int_{\lambda_0}^{\lambda_f} L(x, \dot{x}) d\lambda = \frac{1}{2} \int_{\lambda_0}^{\lambda_f} g_{\mu\nu} \dot{x}^\mu \dot{x}^\nu d\lambda, \quad (37)$$

where L is the Lagrangian and dot represents derivative with respect to the affine parameter λ . For the general static spherically symmetric spacetime in Eq. (1), the Lagrangian is

$$L(x, \dot{x}) = \frac{1}{2} [-A(r)\dot{t}^2 + B(r)^{-1}\dot{r}^2 + r^2(\dot{\theta}^2 + \sin^2\theta\dot{\phi}^2)]. \quad (38)$$

The spherical symmetry allows us to take $\theta = \pi/2$ without the loss of generality. The t and ϕ components of the Euler-Lagrange equation

$$\frac{d}{d\lambda} \left(\frac{\partial L}{\partial \dot{x}^\mu} \right) - \frac{\partial L}{\partial x^\mu} = 0 \quad (39)$$

give us two constants of motion $E = A(r)\dot{t}$ and $L = r^2\dot{\phi}$, which correspond to energy and angular momentum respectively.

For null geodesics we have $g_{\mu\nu}\dot{x}^\mu\dot{x}^\nu = 0$. Hence

$$-A(r)\dot{t}^2 + B(r)^{-1}\dot{r}^2 + r^2\dot{\phi}^2 = 0. \quad (40)$$

After combining the constants of motion with the above equation and using the fact that $\dot{r}^2/\dot{\phi}^2 = (dr/d\phi)^2$, one obtains the orbit equation for null geodesics,

$$\left(\frac{dr}{d\phi} \right)^2 = r^2 B(r) \left(\frac{r^2}{A(r)} \frac{1}{b^2} - 1 \right), \quad (41)$$

where $b = L/E$ is the impact parameter defined as the perpendicular distance, measured at infinity, between the geodesic and the parallel line that passes through the center of black hole in an asymptotically Minkowski spacetime.⁸ The closest distance, R , of the light ray to the black hole is the turning point of the geodesic, where the condition $dr/d\phi|_R = 0$ has to hold. This condition gives us a relation between R and b ,

$$b^2 = \frac{R^2}{A(R)}. \quad (42)$$

When $R = r_{\text{ph}}$, where r_{ph} is the radius of the photon sphere, the light ray that is coming from infinity will orbit around the black hole. In this situation, in addition to $dr/d\phi|_{r_{\text{ph}}} = 0$, the condition $d^2r/d\phi^2|_{r_{\text{ph}}} = 0$ should also hold. Combining these two conditions with Eq. (41) gives

⁸Specifically, the spacetime must be asymptotically flat and the metric must be asymptotically Minkowski so that $A(r) \rightarrow 1$ as $r \rightarrow \infty$.

⁷For a good review of black hole shadow calculations, see [37].

$$\frac{1}{A(r)} \frac{dA(r)}{dr} = \frac{2}{r}, \quad (43)$$

which can be used to determine the radius of the photon sphere. It is easy to show that for the Schwarzschild spacetime, where $A(r) = 1 - 2M_{\text{BH}}/r$, Eq. (43) gives $r_{\text{ph}} = 3M_{\text{BH}}$. Once we determine r_{ph} , we can use Eq. (42) to find the corresponding impact parameter

$$b_{\text{ph}} = \frac{r_{\text{ph}}}{\sqrt{A(r_{\text{ph}})}}. \quad (44)$$

The shadow radius, r_{sh} , turns out to be equal to b_{ph} , because the rays with $b < b_{\text{ph}}$ cannot escape the black hole. It is important, however, to note that b only corresponds to the impact parameter at infinity if we assume the black hole spacetime is asymptotically Minkowski. For asymptotically flat black holes, r_{sh} does not need to be equal to b_{ph} . This can be explained as the following. If the distance between the observer and the center of the black hole is r_o and the angle between r_o and the geodesic at infinity is α , then we can write the relation

$$\sin \alpha = \frac{\mathcal{I}}{r_o}, \quad (45)$$

where \mathcal{I} is the impact parameter. Note that at the observer position, we also have

$$\sin \alpha \sim \left. \frac{\sqrt{r^2 B(r)} d\phi}{dr} \right|_{r_o} \sim \left(b^2 \frac{A(r_o)}{r_o^2} \right)^{1/2} = \left(\frac{R^2}{A(R)} \frac{A(r_o)}{r_o^2} \right)^{1/2}, \quad (46)$$

where we use Eq. (41) and the small angle approximation. The above two equations give

$$\mathcal{I} \sim b \sqrt{A(r_o)}. \quad (47)$$

It is clear that $\mathcal{I} = b$ only when $A(r_o) = 1$. Finally, the black hole shadow size is given by

$$r_{\text{sh}} = \mathcal{I}_{\text{ph}} \sim b_{\text{ph}} \sqrt{A(r_o)} = r_{\text{ph}} \sqrt{\frac{A(r_o)}{A(r_{\text{ph}})}}. \quad (48)$$

Note that the shadow radius is invariant under time rescalings, so that one can obtain the correct result using either \tilde{t} or t .

We now explore how the shadow of a black hole changes in the presence of a DM spike. In an asymptotically Minkowski space, $A(r_o) \approx 1$. For the Schwarzschild case, we find the radius of the shadow to be

$$r_{\text{sh}}^{\text{Schw}} \sim r_{\text{ph}} \sqrt{\frac{1}{A(r_{\text{ph}})}} = 3\sqrt{3}M_{\text{BH}}, \quad (49)$$

where we use the fact that $r_{\text{ph}} = 3M_{\text{BH}}$. In the presence of a DM spike or halo, the asymptotic observer will measure the radius to be

$$r_{\text{sh}}^{\text{SP}} \sim r_{\text{ph}} \sqrt{\frac{1}{\tilde{A}(r_{\text{ph}})}} = r_{\text{ph}} \sqrt{\frac{1}{A(r_{\text{ph}})/\mathcal{C}}} = 3\sqrt{3\mathcal{C}}M_{\text{BH}}. \quad (50)$$

Therefore the black hole shadow radius will appear to be $\sqrt{\mathcal{C}}$ times larger due to the presence of DM. For the shadow radius of M87*, bounds on the DM spike density produce an effect⁹ that is an order of magnitude smaller than is accessible with current Event Horizon Telescope data [22]. In the case of a halo, however, the enlargement of the shadow size is negligible as long as the distribution scale of the halo is within a few orders of magnitude of the value expected from observations (see Fig. 9).

VII. CONCLUSION

We have shown that a DM spike or halo surrounding the black hole at the center of M87 will effect the associated ringdown waveform predominantly in the form of an overall redshift between the frame of an observer who uses the Schwarzschild time below the inner radius of the spike/halo and that of an asymptotic observer. The impact of the redshift on the asymptotic ringdown waveform is significant in case of the spike, but not the halo as long as the distribution scale of the latter is within a few orders of magnitude of the value expected from observations. We conclude that if it becomes possible to detect the gravitational waves associated with perturbations of a galactic black hole with a mass comparable or larger than that of M87*, it could provide the means to detect the presence of a DM spike or put a model dependent bound on its parameters.

We also showed that the presence of a DM spike or halo would increase the black hole shadow radius by the redshift factor of $\sqrt{\mathcal{C}}$. Remarkably, known bounds on the DM spike density produce an effect on the shadow radius of M87* that is just an order of magnitude smaller than is accessible with current Event Horizon Telescope data [22]. Spikes surrounding more massive black holes would produce even larger effects [26] on the shadow and may soon provide the observational means to confirm or rule out their presence.

⁹ $\mathcal{C} \approx 1.004$ for the M87* spike profile provided in Table 2 of [26] for the case of $\alpha_r = 1.94$. This leads to an approximately 0.2% enlargement of the shadow diameter.

ACKNOWLEDGMENTS

We thank Andrei Frolov and Don Page for helpful discussions. G.K. gratefully acknowledges that this research was supported in part by a Discovery Grant from the Natural Sciences and Engineering Research Council of Canada.

APPENDIX: DISCONTINUITY IN POTENTIAL

Here, we derive the discontinuities in the QNM potential that exist at the boundaries of the matter shell. To do this, we first rewrite Eq. (20) as

$$\begin{aligned} \frac{V(r)}{A(r)} &= \frac{l(l+1)}{r^2} + \frac{1}{2r} \left[\left(1 - \frac{2M(r)}{r}\right) \left[\frac{2M(r)}{r(r-2M(r))} \right] + \left(\frac{-8\pi r^2 \rho(r)}{r} + \frac{2M(r)}{r^2} \right) \right] \\ &= \frac{l(l+1)}{r^2} + \frac{1}{2r^2} \left[\frac{2M(r)}{r} + \left(-8\pi r^2 \rho(r) + \frac{2M(r)}{r} \right) \right] \\ &= \frac{l(l+1)}{r^2} + \frac{1}{r^3} [2M(r) - 4\pi r^3 \rho(r)]. \end{aligned} \quad (\text{A3})$$

Therefore,

$$V(r) = A(r) \left[\frac{l(l+1)}{r^2} + \frac{1}{r^3} (2M(r) - 4\pi r^3 \rho(r)) \right] \quad (\text{A4})$$

and since only ρ is discontinuous, the discontinuity in $V(r)$ is

$$\Delta V(r) = -4\pi A(r) \Delta \rho(r). \quad (\text{A5})$$

Using the TOV equations (3) and (4), we can write

$$\begin{aligned} \frac{V(r)}{A(r)} &= \frac{l(l+1)}{r^2} + \frac{1}{2r} \left[B(r) \frac{A'(r)}{A(r)} + B'(r) \right] \\ &= \frac{l(l+1)}{r^2} + \frac{1}{2r} \left[\left(1 - \frac{2M(r)}{r}\right) \mu'(r) + \left(\frac{-2M'(r)}{r} + \frac{2M(r)}{r^2} \right) \right]. \end{aligned} \quad (\text{A2})$$

Thus, the discontinuities in the QNM potential are proportional to the change in matter density at the boundaries, and consequently negligibly small for proposed DM spike profiles [23,26,38].

-
- [1] G. D. Quinlan, L. Hernquist, and S. Sigurdsson, Models of galaxies with central black holes: Adiabatic growth in spherical galaxies, *Astrophys. J.* **440**, 554 (1995).
 - [2] P. Gondolo and J. Silk, Dark matter annihilation at the Galactic center, *Phys. Rev. Lett.* **83**, 1719 (1999).
 - [3] P. Ullio, H. S. Zhao, and M. Kamionkowski, A dark matter spike at the Galactic center?, *Phys. Rev. D* **64**, 043504 (2001).
 - [4] G. Bertone and D. Merritt, Time-dependent models for dark matter at the Galactic center, *Phys. Rev. D* **72**, 103502 (2005).
 - [5] K. Eda, Y. Itoh, S. Kuroyanagi, and J. Silk, New probe of dark-matter properties: Gravitational waves from an intermediate-mass black hole embedded in a dark-matter minispike, *Phys. Rev. Lett.* **110**, 221101 (2013).
 - [6] E. Barausse, V. Cardoso, and P. Pani, Can environmental effects spoil precision gravitational-wave astrophysics?, *Phys. Rev. D* **89**, 104059 (2014); Environmental effects for gravitational-wave astrophysics, *J. Phys. Conf. Ser.* **610**, 012044 (2015).
 - [7] K. Eda, Y. Itoh, S. Kuroyanagi, and J. Silk, Gravitational waves as a probe of dark matter minispikes, *Phys. Rev. D* **91**, 044045 (2015).
 - [8] X.-J. Yue and W.-B. Han, Gravitational waves with dark matter minispikes: The combined effect, *Phys. Rev. D* **97**, 064003 (2018).
 - [9] X.-J. Yue, W.-B. Han, and X. Chen, Dark matter: An efficient catalyst for intermediate-mass-ratio-inspiral events, *Astrophys. J.* **874**, 34 (2019).
 - [10] O. A. Hannuksela, K. C. Y. Ng, and T. G. F. Li, Extreme dark matter tests with extreme mass ratio inspirals, *Phys. Rev. D* **102**, 103022 (2020).
 - [11] B. J. Kavanagh, D. A. Nichols, G. Bertone, and D. Gaggero, Detecting dark matter around black holes with gravitational waves: Effects of dark-matter dynamics on the gravitational waveform, *Phys. Rev. D* **102**, 083006 (2020).
 - [12] A. Chowdhuri, R. K. Singh, K. Kangsabanik, and A. Bhattacharyya, Gravitational radiation from hyperbolic encounters in the presence of dark matter, [arXiv: 2306.11787](https://arxiv.org/abs/2306.11787).

- [13] Z. Arzoumanian *et al.* (NANOGrav Collaboration), The NANOGrav 12.5 yr data set: Search for an isotropic stochastic gravitational-wave background, *Astrophys. J. Lett.* **905**, L34 (2020).
- [14] B. Goncharov *et al.*, On the evidence for a common-spectrum process in the search for the nanohertz gravitational-wave background with the Parkes pulsar timing array, *Astrophys. J. Lett.* **917**, L19 (2021).
- [15] S. Chen *et al.*, Common-red-signal analysis with 24-yr high-precision timing of the European pulsar timing array: Inferences in the stochastic gravitational-wave background search, *Mon. Not. R. Astron. Soc.* **508**, 4970 (2021).
- [16] H. Xu *et al.* (CPTA Collaboration), Searching for the nanohertz stochastic gravitational wave background with the Chinese pulsar timing array data release I, *Res. Astron. Astrophys.* **23**, 075024 (2023).
- [17] J. Antoniadis *et al.*, The second data release from the European pulsar timing array III. Search for gravitational wave signals, *Astron. Astrophys.* **678**, A50 (2023).
- [18] G. Agazie *et al.* (NANOGrav Collaboration), The NANOGrav 15 yr data set: Evidence for a gravitational-wave background, *Astrophys. J. Lett.* **951**, L8 (2023).
- [19] D. J. Reardon *et al.*, Search for an isotropic gravitational-wave background with the Parkes pulsar timing array, *Astrophys. J. Lett.* **951**, L6 (2023).
- [20] Z.-Q. Shen, G.-W. Yuan, Y.-Y. Wang, and Y.-Z. Wang, Dark matter spike surrounding supermassive black holes binary and the nanohertz stochastic gravitational wave background, arXiv:2306.17143.
- [21] The Event Horizon Telescope Collaboration *et al.*, First M87 Event Horizon Telescope results. I. The shadow of the supermassive black hole, *Astrophys. J. Lett.* **875**, L1 (2019).
- [22] L. Medeiros, D. Psaltis, T. R. Lauer, and F. Özel, The image of the M87 black hole reconstructed with PRIMO, *Astrophys. J. Lett.* **947**, L7 (2023).
- [23] S. Nampalliwar, S. Kumar, K. Jusufi, Q. Wu, M. Jamil, and P. Salucci, Modeling the Sgr A* black hole immersed in a dark matter spike, *Astrophys. J.* **916**, 116 (2021).
- [24] K. Jusufi, M. Jamil, P. Salucci, T. Zhu, and S. Haroon, Black hole surrounded by a dark matter halo in the M87 galactic center and its identification with shadow images, *Phys. Rev. D* **100**, 044012 (2019).
- [25] K. Jusufi, M. Jamil, and T. Zhu, Shadows of Sgr A* black hole surrounded by superfluid dark matter halo, *Eur. Phys. J. C* **80**, 354 (2020).
- [26] R. G. Daghigh and G. Kunstatter, Spacetime metrics and ringdown waveforms for galactic black holes surrounded by a dark matter spike, *Astrophys. J.* **940**, 33 (2022).
- [27] Y. Zhao, B. Sun, K. Lin, and Z. Cao, Axial gravitational ringing of a spherically symmetric black hole surrounded by dark matter spike, *Phys. Rev. D* **108**, 024070 (2023).
- [28] L. Hernquist, An analytical model for spherical galaxies and bulges, *Astrophys. J.* **356**, 359 (1990).
- [29] J. F. Navarro, A. Ludlow, and V. Springel, The diversity and similarity of simulated cold dark matter haloes, *Mon. Not. R. Astron. Soc.* **402**, 21 (2010).
- [30] A. D. Ludlow, J. F. Navarro, V. Springel, M. Vogelsberger, J. Wang, S. D. M. White, A. Jenkins, and C. S. Frenk, Secondary infall and the pseudo-phase-space density profiles of cold dark matter haloes, *Mon. Not. R. Astron. Soc.* **406**, 137 (2010).
- [31] C. J. Saxton, Z. Younsi, and K. Wu, Dark matter concentrations in galactic nuclei according to polytropic models, *Mon. Not. R. Astron. Soc.* **461**, 4295 (2016).
- [32] V. Cardoso, K. Destounis, F. Duque, R. Panosso Macedo, and A. Maselli, Black holes in galaxies: Environmental impact on gravitational-wave generation and propagation, *Phys. Rev. D* **105**, L061501 (2022).
- [33] R. A. Konoplya and A. Zhidenko, Solutions of the Einstein equations for a black hole surrounded by a galactic halo, *Astrophys. J.* **933**, 166 (2022).
- [34] D. Merritt and B. Tremblay, The distribution of dark matter in the halo of M87, *Astrophys. J.* **106**, 2229 (1993).
- [35] S. M. Carroll, *Spacetime and Geometry: An Introduction to General Relativity* (Cambridge University Press, Cambridge, England, 2019).
- [36] J. F. Navarro, C. S. Frenk, and S. D. M. White, The structure of cold dark matter halos, *Astrophys. J.* **462**, 563 (1996).
- [37] V. Perlick and O. Yu. Tsupko, Calculating black hole shadows: Review of analytical studies, *Phys. Rep.* **947**, 1 (2022).
- [38] T. Lacroix, M. Karami, A. E. Broderick, J. Silk, and C. Boehm, Unique probe of dark matter in the core of M87 with the Event Horizon Telescope, *Phys. Rev. D* **96**, 063008 (2017).